Research Square

Preprints are preliminary reports that have not undergone peer review.
They should not be considered conclusive, used to inform clinical practice,
or referenced by the media as validated information.

Determination of excitation energy transfer efficiency in individual artificial light- harvesting complexes mimicking chlorosomes

Tomas Malina
Charles University
Ashley M. Hancock
University of Leeds
Sophie A. Meredith
University of Leeds
Peter Kapusta
Czech Academy of Sciences, J. Heyrovský Institute of Physical Chemistry
David Kaftan
Czech Academy of Sciences, Institute of Microbiology
Peter G. Adams
University of Leeds
Jakub Psencik
jakub.psencik@matfyz.cuni.cz

Charles University

Article

Keywords:

Posted Date: August 5th, 2026

DOI: https://doi.org/10.21203/rs.3.rs-10384508/v1

License: This work is licensed under a Creative Commons Attribution 4.0 International License. Read Full License

Additional Declarations: No competing interests reported.

Abstract

Artificial light-harvesting antennas inspired by chlorosomes, the main light-harvesting complexes of green photosynthetic bacteria, represent self-assembling model systems for applications in solar energy conversion. They contain bacteriochlorophyll aggregates with remarkable light-harvesting properties. The pigments are purified from chlorosomes, thus avoiding an expensive chemical synthesis. Here we present results obtained on individual artificial light-harvesting complexes containing bacteriochlorophyll *c* as the main light-harvesting pigment, β-carotene as an aggregation-inducing agent, and bacteriochlorophyll *a* as an acceptor of the harvested energy. We combined multiple microscopic and macroscopic techniques to study free-floating and surface-deposited individual antennas which revealed their structural and functional properties on a single-complex level. The main output is a method which allows the assessment of excitation energy transfer efficiency in individual particles from a small number of detected photons (less than 20 in this work). The data allowed the correlation of the efficiency with the content of β-carotene. Additionally, we determined the size and arrangement of the self-assembled structures, which proved to form rather monodisperse aggregates clustering on the surface. Our method is generally applicable to other types of donor-acceptor systems, from inorganic nanoparticles to molecular assemblies, allowing the study of exciton dynamics in real time at the single-particle level.

Introduction

The growing demand for sustainable energy sources brings more attention to mimicking photosynthesis. Light-harvesting complexes (LHCs) of photosynthetic organisms serve as an inspiration for affordable, non-toxic and biodegradable absorbers that could be used e.g. in solar or photoelectrochemical cells and other systems for solar energy conversion [1, 2]. Natural LHCs are mostly pigment-protein complexes that are difficult to mimic [3, 4]. One exception is a chlorosome, the main LHC of green photosynthetic bacteria, with remarkable light-harvesting properties [5–7]. The natural chlorosome contains self-assembled aggregates of bacteriochlorophyll (BChl) *c*, *d*, or *e* [8, 9] that are surrounded by an envelope containing lipids and proteins. These bacteriochlorophylls form aggregates in aqueous environments *in vitro* without the assistance from protein (or lipids) with properties similar to chlorosomes and represent a promising system for artificial light harvesting [10, 11].

There are three main approaches used to construct artificial light-harvesting complexes: one is based on covalent assemblies (such as arrays or dendrimers of dyes and organic nanocrystals) [12, 13], second on noncovalent assemblies [10, 14–21], and the third one on modified and de novo protein synthesis [3, 4, 22, 23]. Aggregates of chlorosomal BChls belong to the second group. One of their limitations is an insufficient spectral coverage. However, this can be improved by incorporating additional pigments into the aggregate structure, including molecules that do not naturally occur in chlorosomes [24, 25]. Yet, no published work has achieved full coverage of the spectral range between ~ 500–650 nm to date.

Incorporated molecules may also be used to modify other properties. For example, quinones induce excitation quenching in the presence of oxygen [26]. Another option could be the use of plasmonic nanoparticles [27, 28]. The aggregation in aqueous buffers is based on hydrophobic effect and therefore the molecule must be nonpolar in order to be incorporated into the aggregate structure [29]. If extension of spectral coverage is required, the added pigments must not only incorporate into the structure and absorb at required wavelengths but also transfer the captured energy to the aggregates. We have reported such self-assembled artificial antennas based on BChl aggregates and composed of multiple pigments that exhibit an efficient excitation energy transfer between the components previously [30].

The ability to self-organize from multiple components is a key property of artificial light-harvesting systems mimicking chlorosomes such as those using Zn-chlorins [11, 31–33], BChl aggregates enveloped by a polymer surface layer [34], or sheets of nanocrystals [35]. Efforts have been made to control the assembly process [36, 37]. Self-assembled systems offer high pigment density, spectrally broad absorption, and the ability to utilize near-infrared light. However, they often lack environmental stability and need to be kept under anaerobic conditions or the presence of antioxidants [37–39].

Other approaches to artificial light-harvesting offer various advantages and disadvantages compared to BChl aggregates. J-aggregates of (typically) cyanine dyes are more photostable but have a narrow absorption spectrum and suffer from aggregation-induced quenching [40]. Quantum dots (QDs) typically offer spectral tunability, a strong UV absorption with moderate coverage extending into the visible range, and comparable efficiency of EET [41] but often contain acutely toxic compounds [42], although there are efforts towards non-cytotoxic QDs [43–45] and lipid-QD assemblies [46]. Plasmonic particles offer also excellent tunability and, if prepared from gold, are resistant to oxidation and degradation, but function best as enhancers rather than standalone absorbers [47–49].

In bulk samples, the efficiency of excitation energy transfer (EET) between individual components can be determined from steady-state fluorescence spectra. In addition to the classical use of fluorescence excitation spectra [50], we previously presented a method based on fluorescence emission spectra for EET efficiency determination in the case of spectrally overlapping emission of a donor and acceptor [30]. The method is based on a comparison of fluorescence intensity of the donor in the sample with and without the acceptor. However, for single particles, this approach is not applicable because it is impossible to compare the same particle with and without an acceptor. To assess the efficiency for individual antennas, Förster resonance energy transfer equations can be used in various implementations [51–56], but the applicability is often limited to highly luminescent dyes, immobilized samples, multispectral excitation or the necessity to measure single particles labelled by individual donor and acceptor dyes. Methodology to evaluate the efficiency of EET in single particles from a single measurement and with the proper spectral corrections is largely missing.

In this work, we present methodology and results on the determination of EET efficiencies in individual light-harvesting complexes obtained by an alternative method. It is based on integration of fluorescence in two spectral channels (determined by the used band-pass filters) with a dominant contribution from the donor and acceptor, respectively, similar to the ratiometric FRET analysis approach. Our method can provide absolute efficiencies of EET for individual particles, which requires that the spectral sensitivity in each measuring channel is either precisely known or constant. However, this was not possible in our case, so we have further modified the method by including a correction for unknown spectral sensitivity. We have applied the method to artificial LHCs based on BChl *c* aggregates, which contain β-carotene to extend their spectral coverage and BChl *a* as a final acceptor of an excitation energy.

These systems were studied both as particles dispersed in a liquid phase and particles immobilized on a surface. Because the detection sensitivity of the used setups changes dramatically within the measuring channels for these samples, we had to normalize the mean results to bulk data, making the method in effect self-calibrating. The method allows for real-time determination of the efficiency of EET in single particles. It would therefore be possible to use it to study EET in dynamically evolving samples, e.g., during a reaction, assembly, or structural change. The analysis of the data revealed a detailed information about the energy transfer within the assemblies on a single complex level and about their structure. This approach could be applied to any nanoscale system, including natural photosynthetic complexes, inorganic nanoparticles and assemblies of organic molecules.

Results and Discussion

We have studied the efficiency of EET in individual LHCs in aqueous buffer, both floating in solution and immobilized on glass surfaces. For normalization purposes it was necessary to also perform experiments on bulk samples. All fluorescence measurements were performed on samples diluted to absorbance of ~ 0.15 in the Q_y band maximum, and the samples are therefore referred to by the relative β-carotene concentration ratio to BChl *c*, as specified in *Materials and Methods*. The two sample sets with either 0 or 3.75 μM concentrations of BChl *a* are simply referred to as *without* BChl *a* or *with* BChl *a*.

Optical characterization of bulk samples

The prepared BChl *c* aggregates had their Q_y band maximum shifted to approximately 725 nm (compared to 669 nm for BChl *c* in methanol, Fig. 1a) and the Soret band near 450 nm. BChl *c* serves as a donor of the excitation energy in this study. BChl *a* is present in half of the samples as the acceptor of the excitation energy, with its Q_y maximum approximately at 790 nm, the Q_x band close to 600 nm, and the Soret band near 350 nm (Fig. 1c). The other half of the samples do not contain BChl *a* and its BChl *c* emission serves for normalization purposes (Fig. 1b). The absorption spectra of individual components are shown in Fig. 1a. Apart from absorbing light between 400 – 550 nm and transferring excitation energy to BChl *c*, β-carotene is also used because it has been shown to induce aggregation of BChl *c* in aqueous solutions [30, 57]. Here we investigated (on the level of individual complexes) how the efficiency of energy transfer from BChl *c* to BChl *a* is affected by the amount of β-carotene.

The typical bulk fluorescence emission spectra are shown in Fig. 2. The blue curve shows emission of one of the samples without BChl *a* and the orange curve the corresponding sample with BChl *a*. In the same graphs the two spectral channels are shown which were used in single particle experiments with the floating samples along with the dichroic mirror used to separate the signal into the two channels. The channels are determined primarily by the transmission of the two filters, one transmitting mostly BChl *c* emission and the second mostly BChl *a* emission. These spectra were used to determine fractions of the total emission of both pigments in both channels (see SI, *Section 1*, Fig. S1 – 2).

Analysis of particles floating in solution

Fluorescence originated from a small confocal volume (290 nm FWHM in a cross-section) with a structural parameter κ of 5 (ratio of the longitudinal and transverse dimensions of the focal volume). The dilution of samples for fluorescence measurements ensured that the BChl aggregates floated through the confocal volume as individual separated particles, not as a continuum. As a result, most of the time, the recorded time-trace shows no fluorescence signal with single detected photons and occasional flashes corresponding to aggregates floating in and out of the focal volume (Fig. 3a). In every sample, fewer than 20 photons in total were recorded for each individual particle in most detection events (see Fig. S16 in SI).

Data obtained from both detectors were used first to determine the background level in each detection channel. On the arrival time histogram (Fig. 3b), it is possible to see the fluorescence decay after the excitation pulse, which happens roughly between 5 and 10 ns of acquisition time (solid line). The counts in the remaining bins (dotted line) are background originating primarily from detector after-pulsing and dark noise and were considered to be background, which was excluded from the data. This background was also removed from the bins containing signal using maximum likelihood estimation (see SI, *Section 2* and Fig. S3–4).

Then, the Poisson distribution of the background signal was used to set the particle detection threshold in each channel, which corresponds to the probability of false positive detection of 1% (dashed lines in Fig. 3a, for details see SI, *Section 3*).

Finally, the sensitivity correction was determined. Several thousand particles were measured and all photons counted during particle detection were summed for each detection channel. This measured intensity ratio was compared to the expected ratio from steady-state fluorescence spectra, and the sensitivity correction factor was calculated, which was approximately 7.5, differing slightly for each sample (see SI, *Section 4* and Fig. S9). The signal intensity in the 840-nm channel was therefore multiplied by this calculated factor when plotted and is further termed as the corrected signal.

If the sensitivity of detection remained constant within each channel, any fluorophore emitting in both spectral channels would be sufficient for calibration – signal detected in both channels would be compared to what is expected from the same filtered regions in the bulk spectra. Constant sensitivity is often achieved when the spectral channels for fluorescence detection are narrow and in a spectral region not too close to the sensitivity limit of the used setup. However, the sensitivity of our setup was unfortunately not constant

within the selected channels (Fig. S9 in SI, *Section 4*), which means photons arriving at different wavelengths within one channel were detected with different probabilities. This can be corrected for if the total spectral sensitivity of the setup is known, but this total sensitivity changes with every filter, mirror, laser, or detector adjustment. Therefore, a more accessible option is to normalize the average efficiency from all the detected single particles to the bulk efficiency. For a large number of particles these two values should be equal. The procedure is described in detail in the SI, *Section 4*.

The corrected signal for each detected particle was then integrated and used to calculate the efficiency of EET, which was calculated using the following formula:

(1) $$EET = \frac{I_{840\bullet}\,\mathrm{r}^{c}_{750} - I_{750\bullet}\,\mathrm{r}^{c}_{840}}{I_{840\bullet}\,\mathrm{r}^{c}_{750} - I_{750\bullet}\,\mathrm{r}^{c}_{840} + \mathrm{QE}_{a}\left(I_{750\bullet}\,\mathrm{r}^{a}_{840} - I_{840\bullet}\,\mathrm{r}^{a}_{750}\right)}$$

Where $I_{750/840}$ are the corrected fluorescence signals in the selected spectral channels centred around 750 and 840 nm, $\mathrm{r}^{a/c}_{750/840}$ are the fractions of fluorescence from BChl *a* or *c* emitted in the indicated spectral channel vs the intensity of all BChl *a* or *c* signal (these values were determined from the bulk measurements performed between 650–900 nm), respectively (see Fig. S1 in SI, *Section 1*), and QE_{a} is the quantum efficiency of the conversion of excitations into fluorescence at BChl *a* in the detected region (see Fig. S2 in SI, *Section 1*). This formula corrects for the contributions of both fluorophores in both spectral channels. The walkthrough of the derivation of this expression and the five coefficients, which allow us to obtain the efficiency of EET from a single measurement, is provided in SI, *Section 1*.

Results for particles detected in one of the measurements (10% β-carotene with BChl *a*) are shown in Fig. 3c. Multiple measurements of each sample were taken, and cumulative results for EET efficiency of each sample are shown in Fig. 4. In total, the analysis includes 2043 (40 min total measurement time), 6146 (30 min), 9902 (20 min), and 11613 (20 min) particles for samples with 0, 10, 30 and 50% β-carotene content, respectively (all samples contained BChl *a*). The mean signal intensity (brightness) increased with carotenoid content (Fig. S10 in SI, *Section 5*), which aligns with previous bulk results [7, 30]. However, there is a striking difference in the number of detected particles. When recalculated to a number of detected particles per unit time, the difference between the sample with 0% β-carotene (~ 50 detected particles per minute) and 50% β-carotene (~ 580 particles per minute) is more than

10-fold. This cannot be fully explained by the differences in the absorbance at the excitation wavelength (472 nm) due to variable β-carotene contribution (Fig. 1c). There are two possible explanations for this significant difference in the number of detected particles: either the particles get significantly smaller when β-carotene content increases, or there are undetected weakly emitting particles in the samples with low β-carotene content. The latter may be related to the fact that the artificial BChl aggregates have a very low quantum yield, less than 10^{-3} [7].

To address both possibilities, we investigated the particle sizes by comparing the diffusion rates and hydrodynamic diameters of the particles determined by dynamic light scattering (DLS, see Fig. S11–14 and SI, *Section 6*). The method assumes that the studied particles are spherical and reasonably monodisperse. This may not be an entirely accurate assumption, because the DLS-determined dispersity, Đ, ranges between 0.15 and 0.22 for samples measured one day after preparation. The determined Z-average of the measured diameters ranged from 55 to 66 nm (Table S3 in SI, *Section 7*). There was no significant trend indicating a decrease in particle sizes that would explain the increase in number of detected particles. The significant difference in fluorescence intensity between samples despite this similarity in size indicates that there are particles present in the samples undetected in fluorescence measurements.

Evidence of missing particles was originally obtained by fluorescence correlation spectroscopy (FCS), which is intrinsically provided by the nature of the time-resolved fluorescence detection setup. In contrast to the DLS, mean particle sizes determined from FCS are larger, ranging from approximately 150 to 280 nm. The reasons for this discrepancy are related to measurement artifacts discussed in SI, *Section 7*. Nevertheless, results from both DLS and FCS suggest that particle sizes do not decrease with increasing β-carotene content, implying the presence of undetected particles in the samples.

To assess the effects of these undetected particles on the calculated histograms of EET efficiencies, subpopulations of particles were analysed depending on brightness (see SI, *Section 3*, Figures S5–8 and the discussion within the section for details). Calculating the efficiencies for particles of different brightness levels showed that the mean efficiency does not vary between the selected subpopulations. While it could be expected that detecting only bright enough (and likely the largest) particles will result in averaging of the signal, no narrowing of EET efficiency distributions for the brightest subpopulation of particles is observed. This is an important finding revealing that while undetected particles are present in the samples, the efficiencies determined for the detectable particles still represent the whole ensemble.

Another important observation from the EET efficiency histogram is that decreasing β-carotene content across samples yields narrower EET efficiency distributions (Fig. 4). This phenomenon cannot originate from signal averaging, as discussed above. The distribution of efficiencies gets broader with higher carotenoid content, indicating the number of less efficiently transferring particles is increasing. As a result, the average efficiency is decreasing with increasing carotenoid content, as observed for bulk samples previously [30]. While the distribution in samples with high β-carotene concentrations appears shifted to lower values, this change is mostly caused by the increase in particle variability. Even in samples with high β-carotene content, there are many particles with very high efficiency of energy transfer, as is obvious from the overlay in Fig. 4. While for samples with low carotenoid content there are virtually no particles with efficiency of EET from BChl *c* to BChl *a* lower than 0.85, such particles start to appear in samples with higher β-carotene content. We have attributed the decreased efficiency to a larger average distance between BChl *c* and BChl *a* molecules in the aggregates with high carotenoid content. The carotenoids and BChl *a* are likely to compete for the same hydrophobic space between the layers of relatively polar chlorin rings [58].

Analysis of particles immobilized on glass surfaces

The same EET analysis can be used with data collected by FLIM from samples immobilized on a surface. As for floating particles, it was necessary to remove background first (described in SI, *Section 2*). In summary, relevant photon arrival times were selected by time gating (identically to the method for floating particles, Fig. 3b), pixels with 2 or fewer photons were disregarded, and solitary pixels with signal (surrounded by 8 dark pixels) were disregarded as well. The filtered image was then segmented to identify connected pixels containing signal, which were considered to be particles.

Because the signal in the 770-nm detection channel was significantly brighter than in the 840-nm channel (Fig. 5), this filtering and segmentation was applied only to the 770-nm channel. The 840-nm-channel images had dark noise and after-pulsing removed by time gating, but no other filtering was applied. The detected particles from the 770-nm channel were then overlaid over the noise-filtered 840-nm channel image and brightness of particles was determined in the overlaid regions per particle, which ensured an equivalent co-localization approach to detection. Additional FLIM images visually detailing this whole process are shown in the SI, *Section 8* (Fig. S17–20).

In total, we have analysed 933, 1424, 1865, and 173 particles for samples with β-carotene content 0, 1.5, 4.5 and 7.5 μM, respectively, all containing 15 μM BChl *c* and 3.75 μM BChl *a* (Fig. 6). The reason for different numbers of detected particles was that scanned areas were not the same for all samples, and despite the small number of particles detected for the sample with the 7.5 μM β-carotene, the number of detected photons for this sample was higher than for the sample with 0 μM β-carotene. The reasons for this difference in particle brightness are discussed below.

The overall intensity of fluorescence was weaker than for the floating aggregates, and this was especially pronounced for emission from BChl *a*. The corresponding sensitivity correction factor for immobilized samples (i.e. the value required for multiplication of the integrated BChl *a* fluorescence to obtain the same ratio of BChl *c* to BChl *a* fluorescence intensity as for the bulk samples) was almost 50 for the sample without β-carotene and was decreasing with higher carotenoid content to less than 20. In comparison, for all floating aggregates, this sensitivity correction factor was close to 7.5 (for details, see SI, *Section 4*). Since the detector used for FLIM experiments is very similar to the one used for FCS experiments (same model, slightly newer), this significantly different and drastically changing signal ratio indicates surface quenching induced by the contact of the particle with the glass substrate. This quenching affects mostly BChl *a* as the final emitter in the system. This observation is in agreement with previous observations on single chlorosomes, where emission from BChl *a* was only observable from floating chlorosomes and not the deposited ones [59–61]. This selective quenching of BChl *a* indicates that at least some BChl *a* molecules are located close to the surface of the aggregates. Additionally, BChl *a* located more centrally within the aggregate may be quenched by EET to BChl *a* on the aggregate surface. Interestingly, higher β-carotene content suppresses the surface quenching effect. This may happen because of the same reason that increasing β-carotene content lowers the efficiency of EET from BChl *c* to BChl *a*: if β-carotene increases the mean distance between BChls, this could make such an EET from BChl *a* inside the aggregates to the surface BChl *a* less efficient, reducing the effects of surface quenching and increasing the amount of fluorescence radiated from BChl *a* inside the aggregates.

The immobilized particles were often clustered into micrometre-sized deposits. Clusters were not separated in the analysis, as in diffraction-limited images it would not be accurate to do so. Therefore, what is considered a single particle in the analysis is often a cluster of multiple aggregates that were deposited too close together to be distinguished. Clustering should result in averaging of the signals and calculated efficiencies of EET and therefore a

narrower distribution than for floating particles. However, the variable extent of the surface quenching for different particles led to the opposite, giving rise to a wide distribution of measured fluorescence intensities and calculated efficiencies. Additionally, clustering may allow for dense packing of these antennas on surfaces without losing efficiency, provided the surface quenching is either minimized or intentionally used for electron or energy transfer.

As mentioned above, the number of detected particles was lower than for the floating aggregates and the intensity of fluorescence was decreased by the surface quenching. The low number of the detected photons led to quantization of the obtainable efficiencies calculated using the Eq. 1. Despite the use of histogram bins wider than in Fig. 4, some contain systematically lower or higher number of particles because of this shot noise. This is particularly pronounced in the histogram of the sample without β-carotene (Fig. 6a, the bins for 0.77 and 0.85 efficiencies).

The advantage of measuring immobilized samples is that it requires only one detector, because scans can be taken sequentially. However, if using bulk spectra for sensitivity calibration (which was required here, as discussed earlier, see *Floating single particles* and SI, *Section 4*), results become inaccurate if the emission spectra of particles change upon deposition on a surface (which they did, based on the change in ratio of fluorescence intensity between the channels). Because of this change and the surface-induced quenching, the detected fluorescence intensities do not reflect an accurate efficiency of EET anymore. Therefore, for the purpose of analysing the EET efficiency of BChl aggregates on a single particle level, the measurements of floating samples yield significantly more reliable results. Considering future studies: the method for EET efficiency calculation that we have demonstrated would be equally applicable for immobilized samples, if their emission spectra do not change and they do not exhibit surface quenching. An advantage of immobilized samples is that scanning-probe measurements can be performed (described next), which provide information about morphology.

Morphological analysis of particles with AFM and DLS

In fluorescence scans, diffraction-limited images showed particles of up to micrometre scales when deposited on a surface. This observation may originate from morphological flattening of the particle on the surface, increasing its measured diameter due to redistributing its volume onto a plane or from deposition of aggregates in distances shorter than the diffraction limit. Alternatively, particles may cluster on the surface. AFM provided higher resolution to study structural features of individual particles (Fig. 7 and S22–S26 in SI, Section 9).

Measuring the topography of deposited aggregates in AFM images revealed they are composed of smaller aggregate units of approximately 40–100 nm in diameter, clustered together forming a larger assembly of several hundred nanometres across. Due to the statistically small number of the imaged aggregates, the AFM data did not reveal any trend in the sizes observed for aggregates or aggregate units with different pigment composition.

Nevertheless, the size of aggregate units determined by AFM measurements show a remarkable agreement with DLS measurements on particles in liquid. This implies that the particle clusters assemble upon the deposition on the surface, not in the solution. This conclusion is valid for samples observed one day after their preparation. DLS measurements taken two days after preparation showed larger sizes (Table S3 in SI, *Section 7*), indicating that aggregate units may start to cluster even in solution after time.

Although the AFM images show the aggregate units are not perfectly spherical, they may be approximated by a spheroid shape, which further validates the reliability of results obtained from DLS. The observed size also makes

self-assembled BChl aggregates comparable to natural chlorosomes [5, 62], similarly to the BChl *c* aggregates stabilized by an amphiphilic block copolymer [63].

While the aggregates are not as elongated as natural chlorosomes, they appear to have a roughly similar volume. Chlorosomes of *Chlorobaculum tepidum* were reported to contain ~ 50,000-200,000 BChl *c* molecules and measure ~ 155×~75×~25 nm on average, getting smaller when grown under higher light intensity [5, 64, 65], *Chloroflexus aurantiacus* measure approximately ~ 150×~45×~20 nm [5, 66], and *Candidatus chloracidobacterium thermophilum* measure approximately ~ 100×~35×~30 nm [5, 67]. All these bacteria contain BChl *c* as the main light-harvesting pigment with variable amounts of carotenoids, similar to their artificial counterparts. However, most likely due to the lack of the baseplate, the artificial aggregates form more rounded units, as determined by the combination of AFM and DLS analyses.

Conclusions

We have performed a single-particle study of artificial light-harvesting complexes based on BChl *c* aggregates that exhibit very low fluorescence quantum yield (< 0.001 [7]). We were able to determine the efficiencies of energy transfer between BChl *c* and BChl *a* for individual particles composed of co-aggregated BChl *c*, β-carotene, and BChl *a*. These measurements were performed both on free-floating particles in a liquid and on immobilized particles deposited on a surface. Measuring free-floating particles enabled signal collection from a larger number of particles and provided results directly comparable with bulk samples measured in the same medium. Conversely, analysing surface-adsorbed particles permitted longer fluorescence integration times for selected individual particles, as well as repeated measurements of the same particle. However, particles sensitive to surface-induced quenching should be analysed primarily in suspension.

The presence of β-carotene was shown to decrease the overall efficiency of BChl *c* to BChl *a* energy transfer due to increasing its variability. We have shown that the method allows the determination of EET efficiency in individual particles even if they are only weakly luminescent (in this work fewer than 20 photons per particle). To overcome the challenge of accurately assessing photo-active particles that produce such low-level signals required careful image analysis, development of data analysis routines and corrections processes, and we hope that our method can guide future researchers. The method is thus suitable for monitoring of wide range of single particles including natural light-harvesting complexes [68–70], dye-loaded nanoparticles [71], DNA origami systems [72], quantum dot systems [73, 74], liposomal nanoantennas [75] and more. The advantage of our approach is that dynamically evolving systems containing nanoparticles can be monitored and the efficiency of EET in individual nanoparticles can be determined in real time. The final version of our analysis code is provided online for use by other researchers (see Materials & Methods).

In addition, when studying morphology, we discovered that artificial bacteriochlorophyll chlorosome mimics form rather consistent spheroid units which stay dispersed in liquid and cluster into larger particles upon deposition on a surface. Similar analyses of particle size correlated to our method of EET analysis will also be informative for other natural and artificial nanoparticle systems.

Methods

Bulk samples

The samples were prepared by aggregation of BChl *c* with β-carotene and BChl *a* as described previously [30]. Briefly, BChl *c* was isolated from *Chloroflexus aurantiacus*, BChl *a* and β-carotene were purchased from Merck. BChls were dissolved in methanol and β-carotene in anhydrous tetrahydrofuran (THF). Pigments in organic solvents were mixed in desired stoichiometric ratios before injection into 20 mM Tris-HCl buffer (pH 8.0 at 25°C, usually < 30 µl were injected into 3 ml). Two sets of samples were prepared – a set with only BChl *c* and β-carotene and a set with all three pigments. In each set, 15 µM BChl *c* was mixed with 4 different concentrations of β-carotene to prepare different samples, namely 0, 1.5, 4.5, and 7.5 µM (corresponding to 0, 10, 30, and 50% relative to BChl c). The samples in the one set contained no BChl *a* and served as a reference. The samples in the second set contained 3.75 µM BChl *a*. The pigment mixture was prepared to contain the same amount of both methanol and THF no matter what the pigment amount was. The samples were prepared one day ahead and were stored at room temperature in the dark before measurements. Fluorescence emission spectra of the bulk samples were recorded using a Fluorolog QM (Horiba) equipped with double monochromators and R13456 photomultiplier (Hamamatsu).

Fluorescence measurements of floating single particles

Single particle fluorescence emission in liquid phase was recorded on a PicoQuant MicroTime 200 coupled with an Olympus X71 confocal microscope, UPlanSApo 60× 1.2NA objective (Olympus). Samples were excited with a pulsed diode laser at 472 nm (power 2.34 µW and 40 MHz repetition rate, which corresponds to energy of 58.5 fJ and 1.39×10^5 photons per pulse). The excitation power of 2.34 µW was used as the highest intensity where saturation and annihilation effects were not yet apparent while providing the best signal (Fig. S27 in SI, *Section 10*). Signal was collected in epifluorescence mode by the same objective, passed through a 50-µm circular pinhole and detected by two Si avalanche photodiodes (Perkin Elmer SPCM-AQRH-14) in a dual-channel mode. Before detection, a dichroic mirror (FF801_DI02_25x36, Semrock) split the signal into the two channels, and each part of the signal was further filtered using bandpass filters (FF01-747/33 and FF01-842/56, both Semrock). The numbers denote a central wavelength and bandwidth in nm and are later termed simply 750-nm and 840-nm filters, respectively. Signal was detected in a time-correlated single photon counting (TCSPC) mode (so-called time-trace signal) with a 16-ps bin resolution. The full width at half maximum (FWHM) of the instrument response function (IRF) was 332 ± 11 ps in the 750-nm channel and 442 ± 9 ps in the 840-nm channel. The length of the IRF prevented the analysis of fluorescence lifetimes, which were on the order of 20 ps [7].

Fluorescence measurements of immobilized single particles

Immobilized samples were prepared by deposition of the bulk samples on piranha-cleaned glass coverslips coated with poly-L-lysine (PLL, 1 mg/ml, 30-minute incubation) for easier deposition of aggregates. The aggregates in buffer were left to incubate for 30 minutes and then washed repeatedly with clean buffer to remove free-floating aggregates and covered with a layer of clean buffer. Both fluorescence lifetime imaging (FLIM) and atomic force microscopy (AFM) scans were used to characterize samples immersed in a buffer. It was confirmed with AFM that the PLL alone does result in significant additional topography, and that all the detected fluorescence signal originates solely from deposited aggregate samples (Fig. S21 in SI, *Section 9*).

FLIM of immobilized samples was measured using PicoQuant MicroTime 200 with a FlimBee scanner. Samples were excited with a pulsed diode laser at 485 nm (intensity 0.7 µW and 40 MHz repetition rate). Signal was collected in epifluorescence mode by Perkin Elmer SPCM-AQR-14 (25-ps bin resolution) in single-channel detection with FF01-769/41 and FF01-842/56 filters (both Semrock, later termed simply 770-nm and 840-nm filters). The TCSPC measurements were performed as two consecutive scans of the same region with swapped filters, and the order of

used filters was alternated between scans of the same sample. Power dependence was also measured, and it was determined that 0.7 μW is below the limit for a linear response of immobilized samples.

Data analysis for the determination of EET

The details of the analysis are given in the text. The code used for the data analysis was written in MATLAB R2024b and processes the original binary files (PT3 and PTU format for measurements in liquid and in FLIM setup, respectively). The code provided for a single-particle analysis is split into 3 parts: a common part analysing bulk spectra measurements (“Step 1”) and a follow-up code exclusive to either measurements in liquid (“Step 2 (TCSPC in liquid)”) or on surface (“Step 2 (TCSPC on surface FLIM)”).

Code is also provided for fitting autocorrelation functions (ACF) used to calculate the hydrodynamic radii from FCS-detected diffusion. ACFs were first pre-processed using FoCuS_point software [76] and the resulting curves were fitted in MATLAB R2024b with Eq. S6.

The code is available together with the raw data (see the Data Availability section).

Atomic force microscopy (AFM) measurements

Samples for AFM were prepared in the same way as for fluorescence scans of immobilized particles – PLL-coated glass coverslips, measured under 20 mM Tris-HCl buffer. All images were measured in NanoWizard 4 Bio AFM (Bruker, USA) with PFQNM-LC-A-CAL cantilever using Quantitative Imaging Mode at room temperature. Images were scanned at a 128×128 or 256×256 pixel resolution with a line scan speed of 1.2–1.9 Hz and 0.6–0.9 Hz, respectively. The Z-Piezo range was limited to 1.5 μm for best results.

Dynamic light scattering (DLS) measurements

Liquid samples were also measured using DLS to determine the hydrodynamic diameter of the dispersed aggregates. Malvern Panalytical ZetaSizer Nano ZS with a 633 nm He-Ne laser and 173° backscatter detection was used to collect and process data measured on undiluted samples.

Declarations

Competing interests

The author declare no competing interests.

Additional information

Supplementary information is available....

Funding

T.M. and J.P. were supported by Czech Science Foundation (project 26-22037S) and Charles University (project SVV–2025–260832). P.G.A. and A.M.H. were supported by a grant from the Engineering and Physical Sciences Research Council UK (EP/T013958/1). S.A.M. was supported by a PhD studentship from the Biotechnology and Biological Sciences Research Council UK (BBSRC) (BB/M011151/1).

Author Contribution

T.M. – Conceptualisation, Methodology (lead), Formal analysis, Investigation (lead), Code and Data Curation (lead), Writing – Original Draft (lead), Visualisation, Project Administration, Funding acquisition (supporting). A.M.H. – Methodology (supporting), Investigation (supporting), Data Curation (supporting). S.A.M. – Methodology (supporting), Investigation (supporting), Data Curation (supporting). P.K. – Investigation (supporting), Resources. D.K. – Investigation (supporting), Resources. P.G.A. – Conceptualisation, Resources, Supervision, Funding acquisition (lead). J.P. – Conceptualisation, Resources, Writing – Original Draft (supporting), Supervision, Funding acquisition (lead). All authors reviewed and edited the manuscript.

Acknowledgement

The authors thank Dr. David Bina (University of South Bohemia) for providing whole cells of Chloroflexus aurantiacus for pigment purification.

Data Availability

The raw data together with the code used for analysis will be permanently uploaded to Zenodo after review. At this moment, the raw data and the code are available at the following temporary link: https://cunicz-my.sharepoint.com/:f:/g/personal/17311452_cuni_cz/IgA_LAvwTBsWRJHnPgYjErqNAWkloI71Uw6XtwYKfpKmOtQ?e=hQbPWQ

References

1. Wang, C., O'Hagan, M. P., Willner, B. & Willner, I. Bioinspired Artificial Photosynthetic Systems. *Chem-Eur J.* **28**, e202103595 (2022).
2. Voloshin, R. A., Lokteva, E. S. & Allakhverdiev, S. I. Photosystem I in the electrodes. *Curr. Opin. Green. Sust*. **41**, 100816 (2023).
3. Noy, D., Moser, C. C. & Dutton, P. L. Design and engineering of photosynthetic light-harvesting and electron transfer using length, time, and energy scales. *BBA-Bioenergetics* **1757**, 90–105 (2006).
4. Ennist, N. M. et al. De novo design of proteins housing excitonically coupled chlorophyll special pairs. *Nature Chem. Biology* **20** (2024).
5. Adams, P. G. et al. Comparison of the physical characteristics of chlorosomes from three different phyla of green phototrophic bacteria. *BBA-Bioenergetics* **1827**, 1235–1244 (2013).
6. Psencik, J. & Mancal, T. in *in Light harvesting in Photosynthesis*. 121–154 (eds Croce, R., van Grondelle, R., van Amerongen, H. & van Stokkum, I. H. M.) (CRC, 2018).
7. Malina, T., Koehorst, R., Bína, D., Psencík, J. & van Amerongen, H. Superradiance of bacteriochlorophyll aggregates in chlorosomes of green photosynthetic bacteria. *Sci. Rep.* **11**, 8354 (2021).
8. Krasnovsky, A. A. & Bystrova, M. I. Self-assembly of chlorophyll aggregated structures. *BioSystems* 12, 181–194 (1980).
9. Holzwarth, A. R., Griebenow, K. & Schaffner, K. A photosynthetic antenna system which contains a protein-free chromophore aggregate. *Z. Naturforsch C: Biosci.* **45c**, 203–206 (1990).

10. Matsubara, S., Shoji, S. & Tamiaki, H. Biomimetic light-harvesting antennas the self-assembly of chemically programmed chlorophylls. *Chem. Commun.* **60**, 12513–12524 (2024).
11. Mori, Y. & Tamiaki, H. Excitation energy transfer from BODIPY to self-aggregate of zinc bacteriochlorophyll-d analog in supramolecule. *J. Photoch Photobio A*. **464**, 116344 (2025).
12. Chen, H. et al. A Visible-Light-Harvesting Covalent Organic Framework Bearing Single Nickel Sites as a Highly Efficient Sulfur-Carbon Cross-Coupling Dual Catalyst. *Angew Chem. Int. Ed.* **60**, 10820–10827 (2021).
13. Feng, X. et al. Two-dimensional artificial light-harvesting antennae with predesigned high-order structure and robust photosensitising activity. *Sci Rep* 6 (2016).
14. Adams, P. G. et al. Diblock Copolymer Micelles and Supported Films with Noncovalently Incorporated Chromophores: A Modular Platform for Efficient Energy Transfer. *Nano Lett.* **15**, 2422–2428 (2015).
15. Calver, C. F., Schanze, K. S. & Cosa, G. Biomimetic Light-Harvesting Antenna Based on the Self-Assembly of Conjugated Polyelectrolytes Embedded within Lipid Membranes. *Acs Nano*. **10**, 10598–10605 (2016).
16. Shoji, S. & Tamiaki, H. Supramolecular light-harvesting antenna system by co-aggregates of zinc (bacterio)chlorophyll-a derivatives with biomimetic chlorosomal self-assemblies. *Dyes Pigm.* **160**, 514–518 (2019).
17. Meredith, S. A. et al. Model Lipid Membranes Assembled from Natural Plant Thylakoids into 2D Microarray Patterns as a Platform to Assess the Organization and Photophysics of Light-Harvesting Proteins. *Small* **17**, 2006608 (2021).
18. Hancock, A. M. et al. Enhancing the spectral range of plant and bacterial light-harvesting pigment-protein complexes with various synthetic chromophores incorporated into lipid vesicles. *J. Photoch Photobio B*. **237**, 112585 (2022).
19. Liu, J. H., Sun, J. L., Pan, C. H. & Yang, G. Z. The Materials and Application of Artificial Light Harvesting System Based on Supramolecular Self-assembly. *Chemistryselect* **8**, e202202979 (2023).
20. Kondo, M., Hancock, A. M., Kuwabara, H., Adams, P. G. & Dewa, T. Photocurrent Generation by Plant Light-Harvesting Complexes is Enhanced by Lipid-Linked Chromophores in a Self-Assembled Lipid Membrane. *J. Phys. Chem. B*. **129**, 900–910 (2025).
21. Rousseau, A. et al. Exciton-Diffusion Enhanced Energy Capture in an Integrated Nanoscale Platform. *Acs Nano*. **19**, 14865–14872 (2025).
22. Zhao, L. L. et al. Enzyme-Triggered Defined Protein Nanoarrays: Efficient Light-Harvesting Systems to Mimic Chloroplasts. *Acs Nano*. **11**, 938–945 (2017).
23. Li, X. M. et al. Template-Free Construction of Highly Ordered Monolayered Fluorescent Protein Nanosheets: A Bioinspired Artificial Light-Harvesting System. *Acs Nano*. **13**, 1861–1869 (2019).
24. Alster, J. et al. Self-assembly and energy transfer in artificial light-harvesting complexes of bacteriochlorophyll c with astaxanthin. *Photosynth Res.* **111**, 193–204 (2012).
25. Matenova, M. et al. Energy transfer in aggregates of bacteriochlorophyll c self-assembled with azulene derivatives. *Phys. Chem. Chem. Phys.* **16**, 16755–16764 (2014).
26. Alster, J., Zupcanova, A., Vacha, F. & Psencik, J. Effect of quinones on formation and properties of bacteriochlorophyll c aggregates. *Photosynth Res.* **95**, 183–189 (2008).
27. Peedikakkandy, L. et al. On the nature of plasmon-induced photocurrent enhancement in Bacteriochlorophyll sensitized solar cells: Towards red light harvesting. *Mater. Chem. Phys.* **258**, 123932 (2021).

28. Donahue, E., Malina, T., Smith, E., Psencík, J. & Sprague-Klein, E. A. Photophysics of plasmonically enhanced self-assembled artificial light-harvesting nanoantennas. *Commun. Chem.* **8**, 263 (2025).
29. Zupcanova, A. et al. The length of esterifying alcohol affects the aggregation properties of chlorosomal bacteriochlorophylls. *Photochem. Photobiol*. **84**, 1187–1194 (2008).
30. Malina, T., Bina, D., Collins, A. M., Alster, J. & Pšenčík, J. Efficient two step excitation energy transfer in artificial light harvesting antenna based on bacteriochlorophyll aggregates. *J. Photochem. Photobiol B*. **254**, 112891 (2024).
31. Ocakoglu, K., Joya, K. S., Harputlu, E., Tarnowska, A. & Gryko, D. T. A nanoscale bio-inspired light-harvesting system developed from self-assembled alkyl-functionalized metallochlorin nano-aggregates. *Nanoscale* **6**, 9625–9631 (2014).
32. Shoji, S., Ogawa, T., Hashishin, T. & Tamiaki, H. Self-Assemblies of Zinc Bacteriochlorophyll-d Analogues Having Amide, Ester, and Urea Groups as Substituents at 17-Position and Observation of Lamellar Supramolecular Nanostructures. *Chemphyschem* **19**, 913–920 (2018).
33. Shoji, S., Nomura, Y. & Tamiaki, H. Heterodimers of zinc and free-base chlorophyll derivatives co-assembled in biomimetic chlorosomal J-aggregates. *Photochem. Photobiol. Sci.* **18**, 555–562 (2019).
34. Orf, G. S. et al. Polymer-Chlorosome Nanocomposites Consisting of Non-Native Combinations of Self-Assembling Bacteriochlorophylls. *Langmuir* **33**, 6427–6438 (2017).
35. Chen, P. Z. et al. Light-Harvesting Systems Based on Organic Nanocrystals To Mimic Chlorosomes. *Angew Chem. Int. Ed.* **55**, 2759–2763 (2016).
36. Matsubara, S. & Tamiaki, H. Phototriggered Dynamic and Biomimetic Growth of Chlorosomal Self-Aggregates. *J. Am. Chem. Soc.* **141**, 1207–1211 (2019).
37. Matsubara, S. & Tamiaki, H. Supramolecular chlorophyll aggregates inspired from specific light-harvesting antenna chlorosome: Static nanostructure, dynamic construction process, and versatile application. *J. Photochem. Photobiol C*. **45**, 100385 (2020).
38. Otsuki, J. Supramolecular approach towards light-harvesting materials based on porphyrins and chlorophylls. *J. Mater. Chem. A*. **6**, 6710–6753 (2018).
39. Buscemi, G., Vona, D., Trotta, M., Milano, F. & Farinola, G. M. Chlorophylls as Molecular Semiconductors: Introduction and State of Art. *Adv. Mater. Technol-Us*. **7**, 2100245 (2022).
40. Safar Sajadi, S. M. & Khoee, S. The simultaneous role of porphyrins' H- and J- aggregates and host-guest chemistry on the fabrication of reversible Dextran-PMMA polymersome. *Sci. Rep.* **11**, 2832 (2021).
41. Hao, M. M., Ding, S. S., Gaznaghi, S., Cheng, H. Y. & Wang, L. Z. Perovskite Quantum Dot Solar Cells: Current Status and Future Outlook. *Acs Energy Lett.* **9**, 308–322 (2024).
42. Pelley, J. L., Daar, A. S. & Saner, M. A. State of Academic Knowledge on Toxicity and Biological Fate of Quantum Dots. *Toxicol. Sci.* **112**, 276–296 (2009).
43. Xu, X. Y. et al. Electrophoretic analysis and purification of fluorescent single-walled carbon nanotube fragments. *J. Am. Chem. Soc.* **126**, 12736–12737 (2004).
44. Li, K. et al. Biocompatible organic dots with aggregation-induced emission for and fluorescence imaging. *Sci. China Chem.* **56**, 1228–1233 (2013).
45. Wang, L., Weng, S. J., Su, S. & Wang, W. W. Progress on the luminescence mechanism and application of carbon quantum dots based on biomass synthesis. *Rsc Adv.* **13**, 19173–19194 (2023).

46. Whipp, J. T., Hancock, A. M., Aslam, Z., Critchley, K. & Adams, P. G. Analysis of lipid-assisted self-assembly of hydrophobic CuInS/ZnS quantum dots into water-stable nanoclusters that perform intra-cluster energy transfer. *Nanoscale* (2026).
47. Alkhalayfeh, M. A., Aziz, A. A. & Pakhuruddin, M. Z. An overview of enhanced polymer solar cells with embedded plasmonic nanoparticles. *Renew. Sust Energ. Rev.* **141**, 110726 (2021).
48. Kaur, N., Singh, D. P. & Mahajan, A. Plasmonic Engineering of TiO2 Photoanodes for Dye-Sensitized Solar Cells: A Review. *J. Electron. Mater.* **51**, 4188–4206 (2022).
49. Du, X. Y., Liu, L. Q. & Ye, J. H. Plasmonic Metal Nanoparticles for Artificial Photosynthesis: Advancements, Mechanisms, and Perspectives. *Sol Rrl*. **5**, 2100611 (2021).
50. Blankenship, R. E. Molecular mechanisms of photosynthesis, Edn. Third editionWiley, Hoboken;. (2021).
51. Lakowicz, J. R. *Principles of fluorescence spectroscopy, Edn. 3rd* (Springer, 2006).
52. Pons, T., Medintz, I. L., Wang, X., English, D. S. & Mattoussi, H. Solution-phase single quantum dot fluorescence resonance energy transfer. *J. Am. Chem. Soc.* **128**, 15324–15331 (2006).
53. Roszik, J., Lisboa, D., Szöllosi, J. & Vereb, G. Evaluation of Intensity-Based Ratiometric FRET in Image Cytometry-Approaches and a Software Solution. *Cytom Part. A*. **75a**, 761–767 (2009).
54. Hellenkamp, B. et al. Precision and accuracy of single-molecule FRET measurements-a multi-laboratory benchmark study (15, pg 984, 2018). *Nat. Methods*. **15**, 984–984 (2018).
55. Phelps, C., Huang, T., Wang, J. & Nan, X. L. Multipair Förster Resonance Energy Transfer via Spectrally Resolved Single-Molecule Detection. *J. Phys. Chem. B*. **126**, 5765–5771 (2022).
56. Agam, G. et al. Reliability and accuracy of single-molecule FRET studies for characterization of structural dynamics and distances in proteins. *Nat Methods* **20** (2023).
57. Alster, J. et al. beta-Carotene to bacteriochlorophyll c energy transfer in self-assembled aggregates mimicking chlorosomes. *Chem. Phys.* **373**, 90–97 (2010).
58. Bily, T. et al. Planar arrangement of bacteriochlorophyll aggregates in chlorosomes of. *Biophys. J.* **125**, 1494–1505 (2026).
59. Shibata, Y., Saga, Y., Tamiaki, H. & Itoh, S. Low-temperature fluorescence from single chlorosomes, photosynthetic antenna complexes of green filamentous and sulfur bacteria. *Biophys. J.* **91**, 3787–3796 (2006).
60. Saga, Y. et al. Spectral heterogeneity in single light-harvesting chlorosomes from green sulfur photosynthetic bacterium Chlorobium tepidum. *Photochem. Photobiol*. **75**, 433–436 (2002).
61. Saga, Y. et al. Fluorescence emission spectroscopy of single light-harvesting complex from green filamentous photosynthetic bacteria. *J. Phys. Chem. B*. **106**, 1430–1433 (2002).
62. Martinez-Planells, A. et al. Determination of the topography and biometry of chlorosomes by atomic force microscopy. *Photosynth Res.* **71**, 83–90 (2002).
63. Collins, A. M., Timlin, J. A., Anthony, S. M. & Montano, G. A. Amphiphilic block copolymers as flexible membrane materials generating structural and functional mimics of green bacterial antenna complexes. *Nanoscale* **8**, 15056–15063 (2016).
64. Montano, G. A. et al. Characterization of *Chlorobium tepidum* chlorosomes: A calculation of bacteriochlorophyll *c* per chlorosome and oligomer modeling. *Biophys. J.* **85**, 2560–2565 (2003).
65. Psencik, J., Butcher, S. J. & Tuma, R. in The Structural Basis of Biological Energy Generation, Vol. 39. (ed. M.F. Hohmann-Marriott) 77–109Springer, Dordrecht; (2014).

66. Psencik, J. et al. Structure of chlorosomes from the green filamentous bacterium *Chloroflexus aurantiacus*. *J. Bacteriol.* **191**, 6701–6708 (2009).
67. Costas, A. M. G. et al. Ultrastructural Analysis and Identification of Envelope Proteins of Candidatus Chloracidobacterium thermophilum Chlorosomes. *J. Bacteriol.* **193**, 6701–6711 (2011).
68. Squires, A. H. & Moerner, W. E. Direct single-molecule measurements of phycocyanobilin photophysics in monomeric C-phycocyanin. *Proc. Natl. Acad. Sci.* 114, 9779–9784 (2017).
69. Mascoli, V., Gelzinis, A., Chmeliov, J., Valkunas, L. & Croce, R. Light-harvesting complexes access analogue emissive states in different environments. *Chem. Sci.* **11**, 5697–5709 (2020).
70. Manna, P., Davies, T., Hoffmann, M., Johnson, M. P. & Schlau-Cohen, G. S. Membrane-dependent heterogeneity of LHCII characterized using single-molecule spectroscopy. *Biophys. J.* **120**, 3091–3102 (2021).
71. Biswas, S., Niedzwiedzki, D. M. & Pakrasi, H. B. Energy dissipation efficiency in the CP43 assembly intermediate complex of photosystem II. *Biochim. Biophys. Acta Bioenerg*. **1864**, 148982 (2023).
72. Olejko, L. & Bald, I. FRET efficiency and antenna effect in multi-color DNA origami-based light harvesting systems. *Rsc Adv.* **7**, 23924–23934 (2017).
73. Jung, S. & Chen, X. Y. Quantum Dot-Dye Conjugates for Biosensing, Imaging, and Therapy. *Adv. Healthc. Mater.* **7**, 1800252 (2018).
74. Demers, S. M. E., Kuhne, W. W., Swindle, A. R., Dick, D. D. & Coopersmith, K. J. Quantum Dot-DNA FRET Conjugates for Direct Analysis of Methylphosphonic Acid in Complex Media. *Acs Omega*. **8**, 23017–23023 (2023).
75. Hancock, A. M., Meredith, S. A., Connell, S. D., Jeuken, L. J. C. & Adams, P. G. Proteoliposomes as energy transferring nanomaterials: enhancing the spectral range of light-harvesting proteins using lipid-linked chromophores. *Nanoscale* **11**, 16284–16292 (2019).
76. Waithe, D., Clausen, M. P., Sezgin, E. & Eggeling, C. FoCuS-point: software for STED fluorescence correlation and time-gated single photon counting. *Bioinformatics* **32**, 958–960 (2016).

Figures

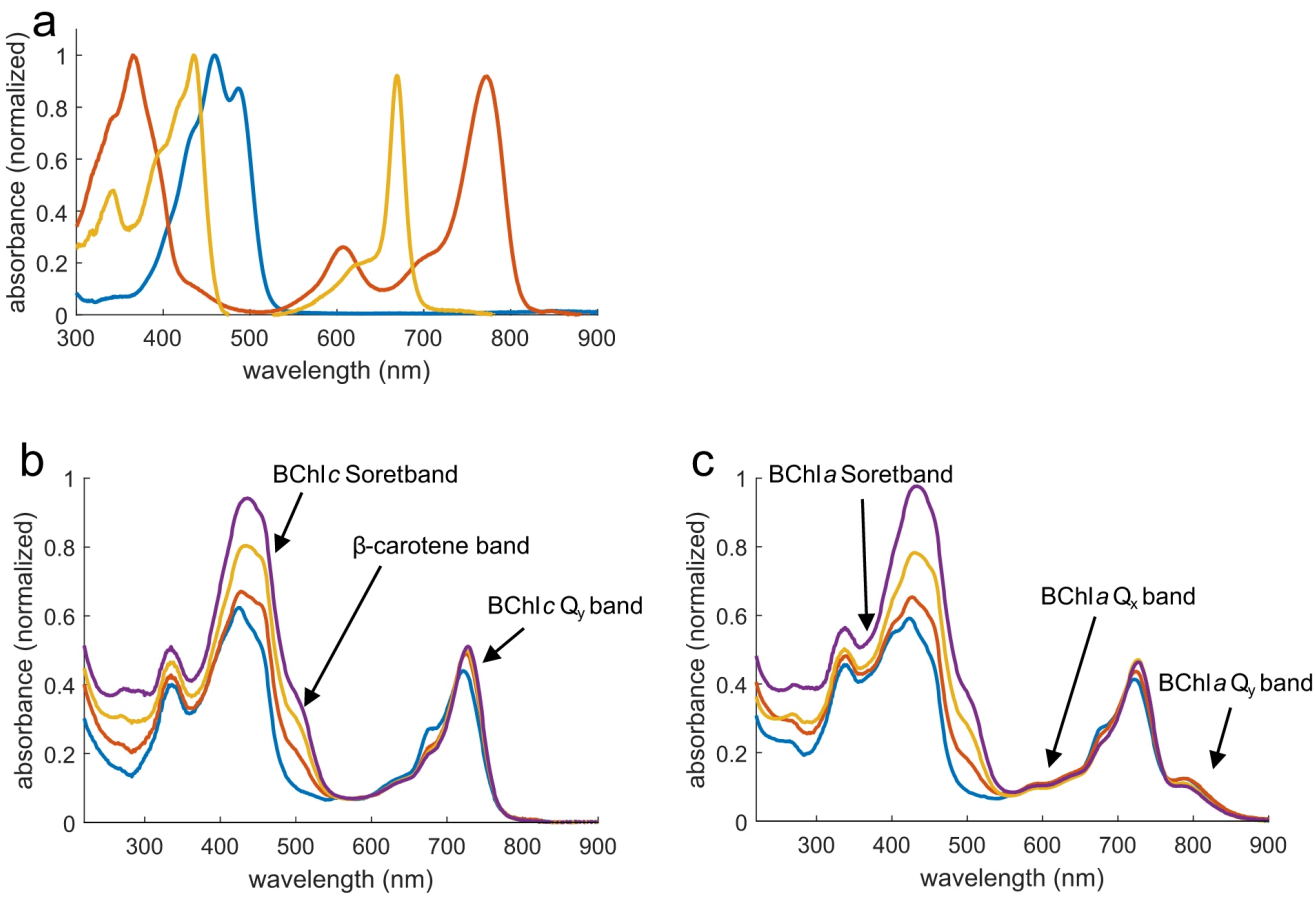


Figure 1

(a) Absorption spectra of individual pigments used for the preparation of aggregate samples – monomeric BChl *c* in methanol (yellow), β-carotene in THF (blue), and BChl *a* in methanol (orange). (b-c) Absorption spectra of the bulk samples containing four different β-carotene concentrations, diluted for fluorescence measurements. (b) Aggregates containing only BChl *c* and β-carotene. The starting samples all contained 15 μM BChl *c* and either 0, 1.5, 4.5 or 7.5 μM β-carotene (blue, orange, yellow, purple, respectively) but some BChl *c* was lost during assembly (as described in the text). (c) The corresponding aggregate samples to (b) with the addition of BChl *a* (3.75 μM BChl *a*). The spectra in panels (b-c) were normalized to the area of the BChl *c* Q_y band.

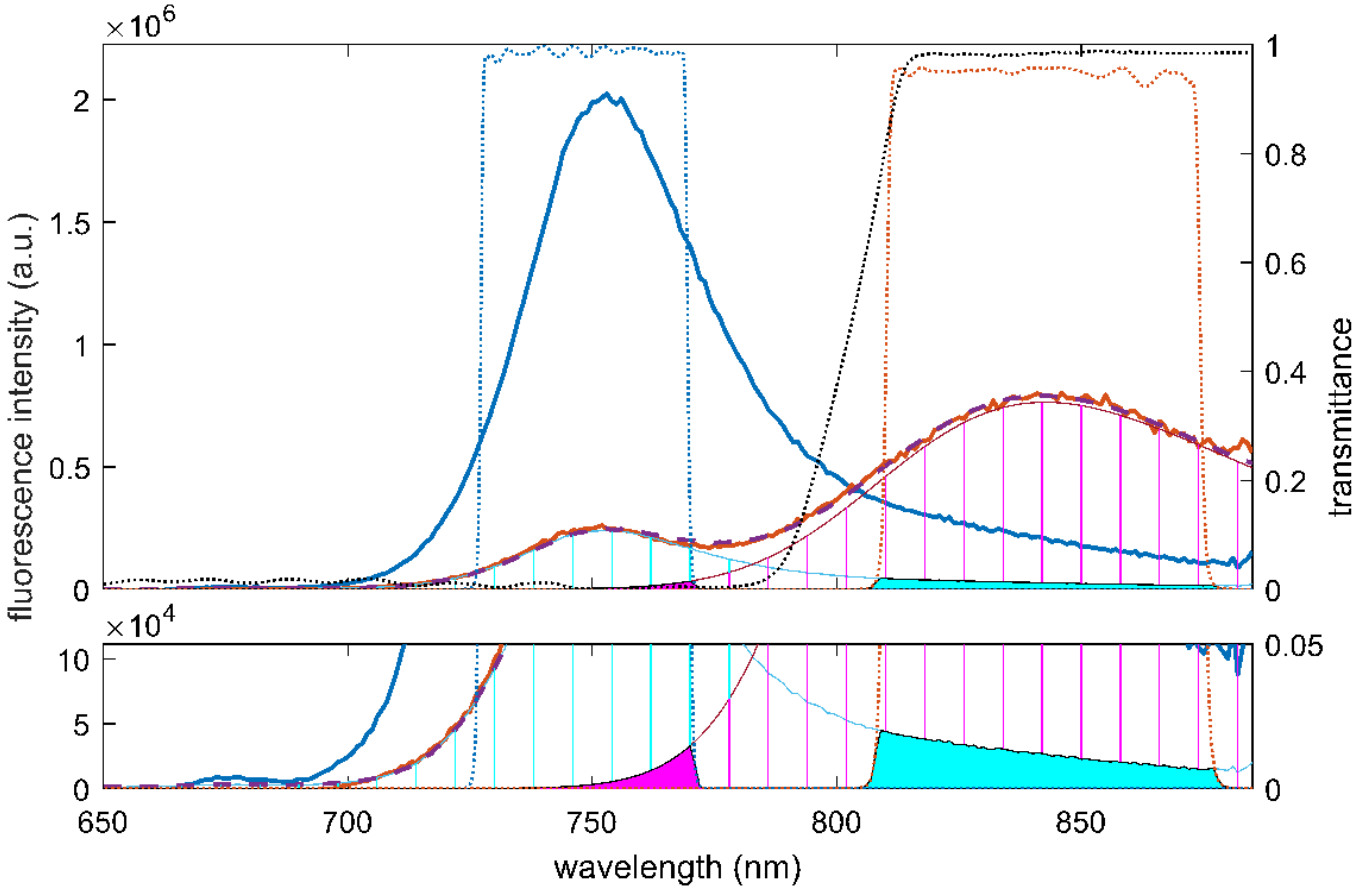


Figure 2

Steady-state fluorescence emission of artificial aggregates of BChl *c* and β-carotene (blue, donor sample, D) and BChl *c*, β-carotene and BChl *a* (orange, donor + acceptor sample, D+A). The components in the D+A spectrum are fitted with the D spectrum (cyan + striped area) and a skewed gaussian (magenta + striped area) [30]. The combined fit (cyan + magenta) is shown in dashed purple. The dotted lines show the transmittances of the dichroic mirror and spectral filters used to separate the signal into two detection channels. Filled areas (cyan at ~810–880 nm and magenta at ~750–770 nm) represent fluorescence of the donor/acceptor leaking into the detection channels where mainly acceptor/donor contributes, respectively, which need to be corrected for (see SI, *Section 1*). The bottom panel shows the leaking contributions with a magnified y-axis.

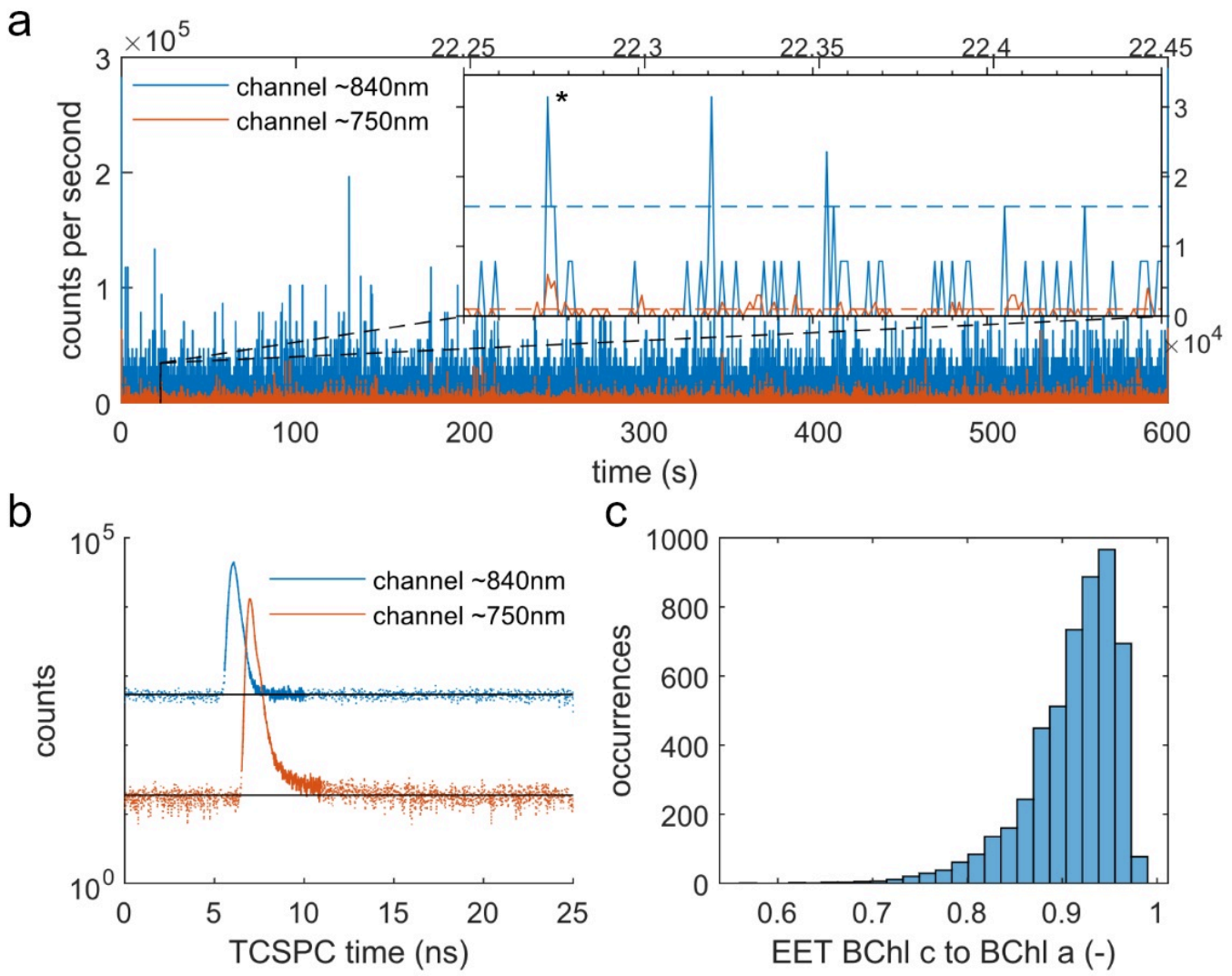


Figure 3

One measurement of aggregates containing BChl *a* and 30% β-carotene relative to BChl *c*. (a) The corrected time-trace signal composed from the signal within relevant signal bins shows fluctuations of intensity when particles float through the confocal volume at a sampling rate of 1 ms. The coloured dashed lines show the thresholds for peak detection in each spectral channel corresponding to the false-positive detection threshold of 1% determined by the Poisson distribution of noise. Only co-localized detection events (i.e. simultaneous detections in both channels) are registered as particles. In this inset, only the peak marked with * is counted towards detected particles. (b) Photon arrival-time histogram with a highlighted relevant signal region (solid blue and orange lines) and the irrelevant photon arrival times (dotted lines), fitted with maximum likelihood estimation for background (black lines). (c) For each particle in this measurement, the efficiency of energy transfer was determined, and the histogram of the calculated efficiencies is shown.

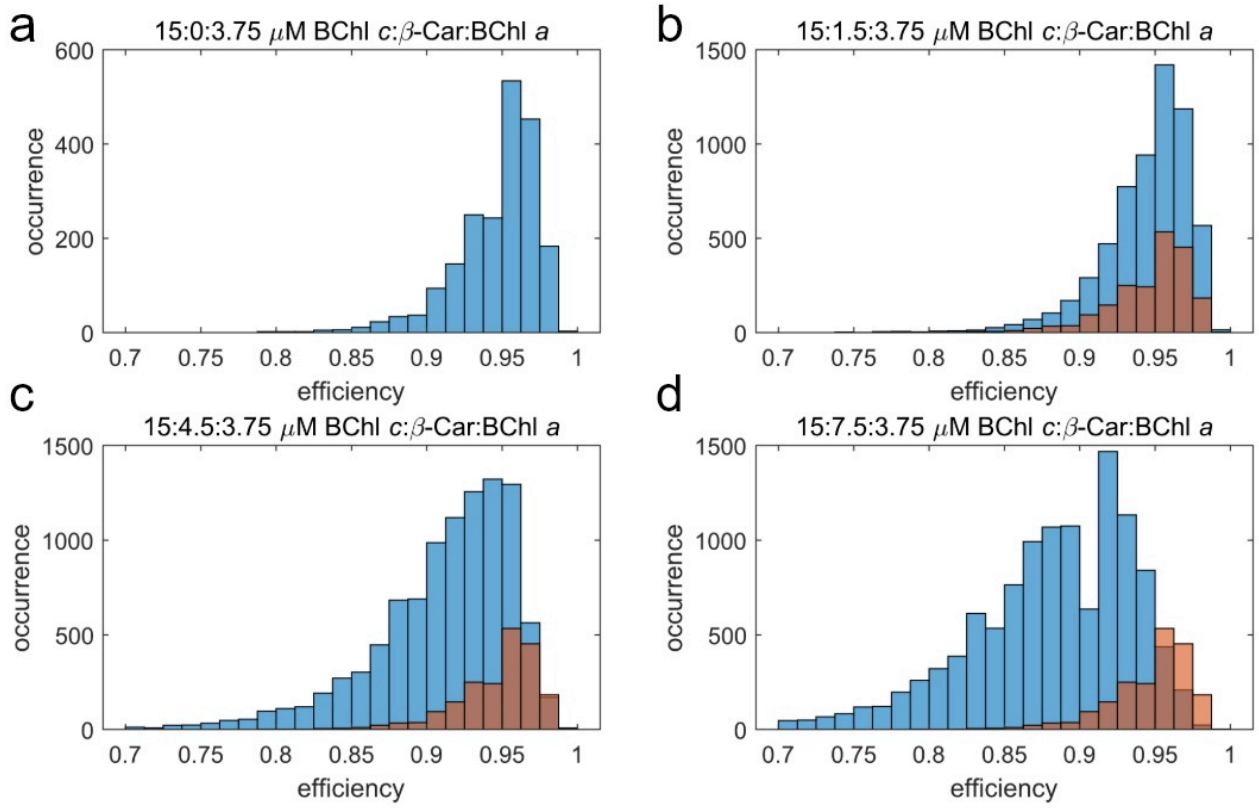


Figure 4

Histograms of efficiencies of EET from BChl *c* to BChl *a* in aggregates with varying concentration of β-carotene measured from single-particle analysis in the liquid phase. In panels b-d, the distribution for the sample without β-carotene (i.e., the data from panel a) is overlaid in orange. The histogram bin width for efficiency is 0.0125, for all panels.

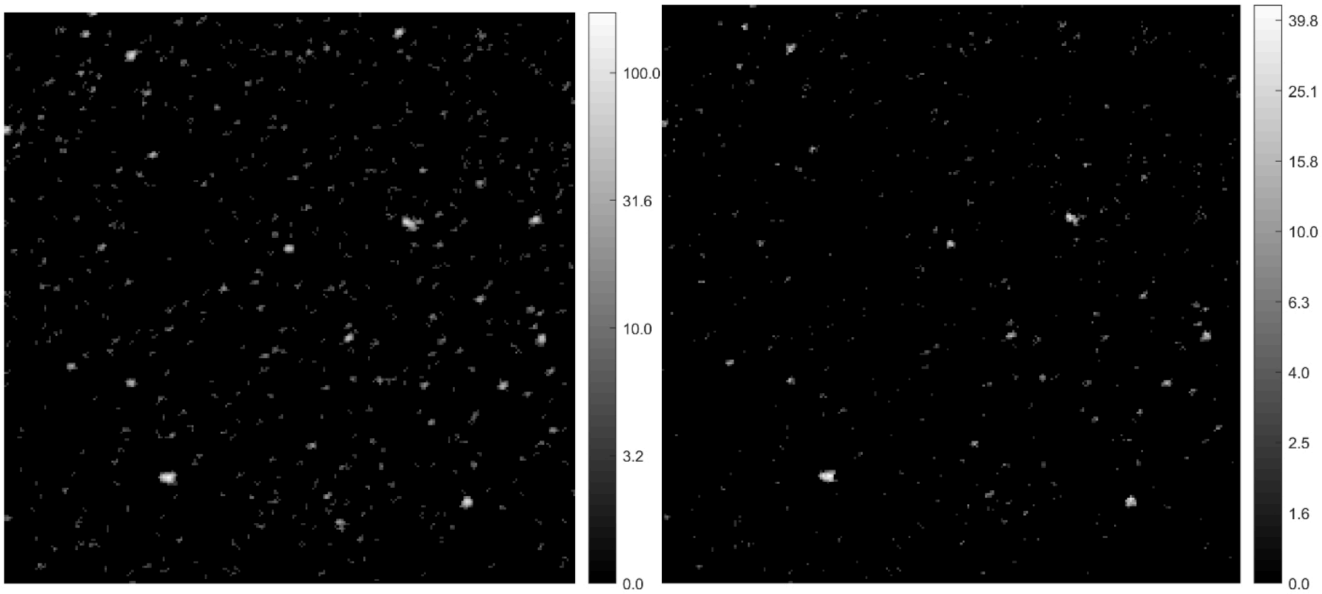


Figure 5

Example FLIM scan of aggregates with 15 µM BChl *c*, 1.5 µM β-carotene and 3.75 µM BChl *a*, immobilized on a glass substrate. Left: fully filtered 770-nm channel, right: noise-filtered 840-nm channel with applied binary mask created from 770-nm channel. Both images: 25x25 µm, 256 × 256 pixels, logarithmic brightness.

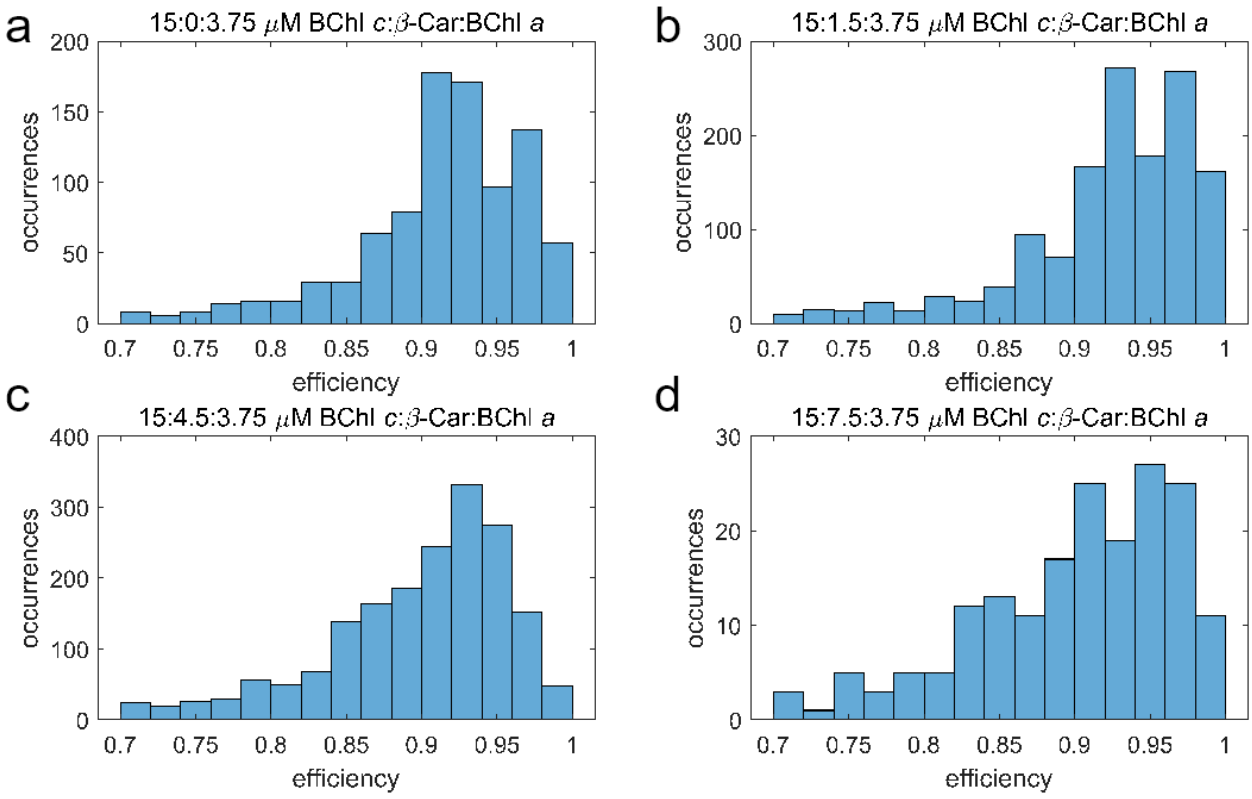


Figure 6

Histograms of calculated EET efficiencies from BChl *c*to BChl *a* in aggregates with varying concentration of β-carotene immobilized on glass surfaces. The values are strongly affected by surface quenching and therefore the histograms are not representative of real EET efficiency values. The histograms bin width for efficiency is 0.02, for all panels.

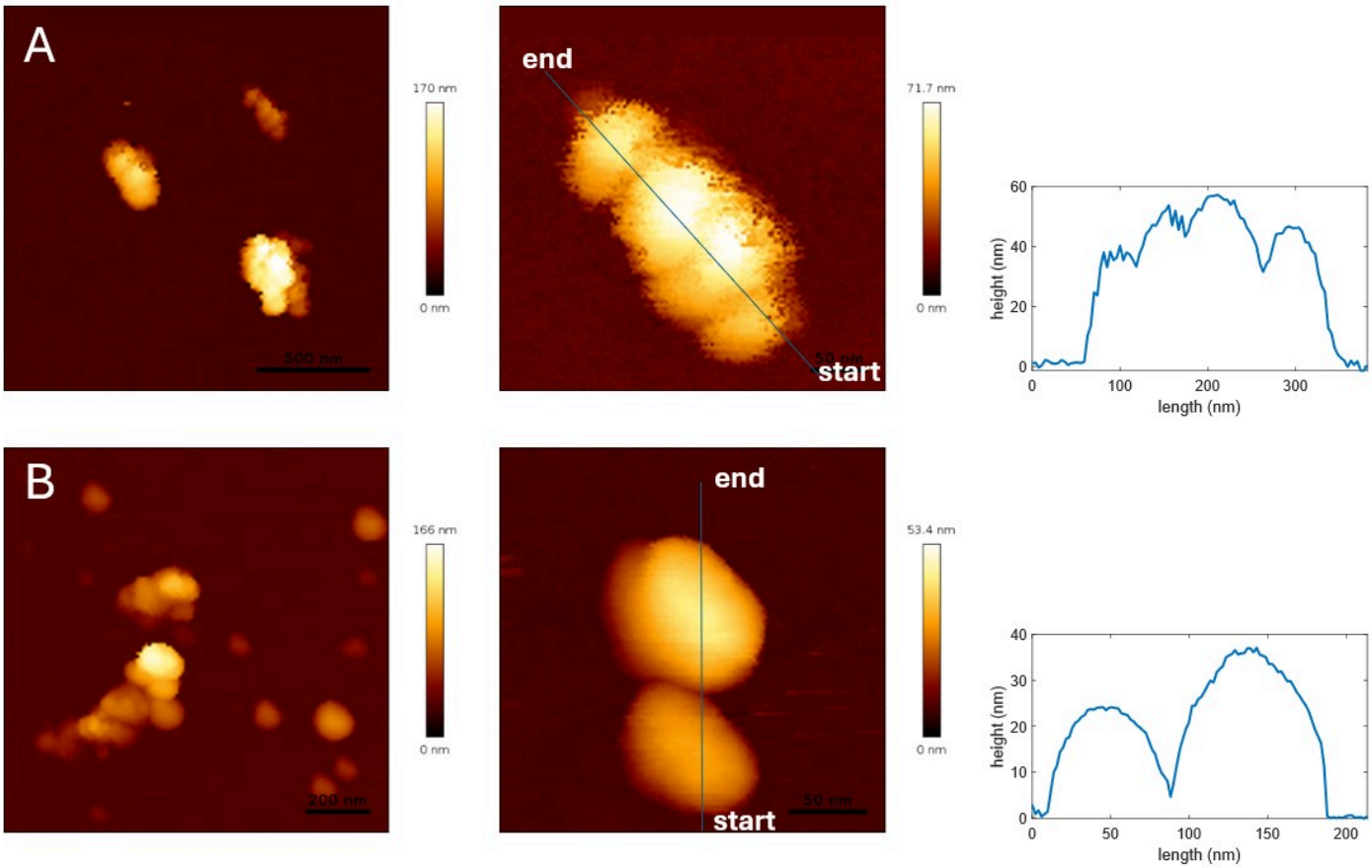


Figure 7

AFM topographs of aggregates with and without BChl *a*. Particles were adsorbed to a glass surface and imaged under liquid (20 mM Tris-HCl buffer, pH 8.0). (A) Example images of aggregates with 15 µM BChl *c*, 4.5 µM β-carotene and 3.75 µM, BChl *a*. A height profile (graph, right) is shown to better visualise the clustering of individual aggregate units. (B) Example images of aggregates with 15 µM BChl *c* and 1.5 µM β-carotene (without BChl *a*).

Supplementary Files

This is a list of supplementary files associated with this preprint. Click to download.

- JHINSTLeedsms13SIfinSR.pdf